SCIENCE CHINA
Chemistry

•ARTICLES•
SPECIAL ISSUE: 2025 Emerging Investigator Issue

December 2025 Vol.68 No.12: 6591–6599
https://doi.org/10.1007/s11426-025-3087-0

Dynamic covalent assembly of low-symmetry chiral organic nanotubes via disulfide-bridged pillar[5]arene dimerization

Ping Li, Kai Lan, Xiaobo Zhang, Hanchi Zhong & Chuyang Cheng*

College of Chemistry, Key Laboratory of Green Chemistry and Technology of Ministry of Education, Sichuan University, Chengdu 610064, China

Received September 12, 2025; accepted October 20, 2025; published online November 6, 2025

Organic nanotubes have garnered significant attention over recent decades due to their potential applications across various fields. Despite this, the synthesis of stable organic nanotubes with precise stereochemical control remains challenging. While dynamic covalent chemistry has proven to be a powerful tool for efficiently constructing stable organic nanotubes, precise stereochemical control of low-symmetry chiral nanotubes is still an area requiring further exploration. Here we report the synthesis of a low-symmetry chiral organic nanotube through dynamic covalent self-assembly of a rim-differentiated pentathiol-functionalized pillar[5]arene (**p5-SH**). Dimerization of this highly symmetric building block generates a covalently linked low-symmetry organic nanotube (**[p5-S]$_2$**). A pair of enantiomers, ***P′M*-[p5-S]$_2$** and ***M′P*-[p5-S]$_2$**, was separated and characterized. The assembly and disassembly of **[p5-S]$_2$** are redox-regulated, with disulfide bonds functioning as molecular switches. Furthermore, the synergistic effects of dual pillar[5]arene cavities in **[p5-S]$_2$** create a deep cavity with a rigid asymmetric architecture. This structure significantly enhances the nanotube's ability to recognize linear alkyl chains in solution, making it a promising candidate for various applications in materials science and nanotechnology.

organic nanotubes, pillararene, disulfide bond, dynamic covalent chemistry, host-guest chemistry

Citation: Li P, Lan K, Zhang X, Zhong H, Cheng C. Dynamic covalent assembly of low-symmetry chiral organic nanotubes via disulfide-bridged pillar[5]arene dimerization. *Sci China Chem*, 2025, 68: 6591–6599, https://doi.org/10.1007/s11426-025-3087-0

1 Introduction

Nanotubes have emerged as fascinating one-dimensional hollow structures owing to their intriguing physical and chemical properties, as well as their broad applications in nanotechnology [1], electronics [2,3], molecular sensing [4–6], and biomedicine [7,8]. While carbon nanotubes dominate this field, organic nanotubes offer distinct advantages, including structural tunability [9–12], facile functionalization, and biocompatibility [13–17]. Despite these advances, the precise synthesis of organic nanotubes with controlled diameters and chirality remains a formidable challenge, primarily due to the inherent limitations of non-covalent supramolecular assembly strategies in achieving structural stability and precise stereochemical control [18–22]. Covalent approaches, on the other hand, though providing enhanced stability, often lack the dynamic reversibility required for error correction during nanotube elongation [23–26]. This dichotomy highlights the potential of dynamic covalent chemistry (DCC) [27–30], which combines the robustness of covalent bonds with self-repairing capabilities (Figure 1a). Among DCC systems, disulfide linkages [31–35] stand out for their redox-responsive reversibility and conformational adaptability that can tolerate significant twisting, offering dual functionality as both structural connectors and conformational modulators (Figure 1b).

Macrocyclic molecules exhibit unique advantages in

*Corresponding author (email: cycheng@scu.edu)

© Science China Press 2025

https://www.sciengine.com/doi/10.1007/s11426-025-3087-0

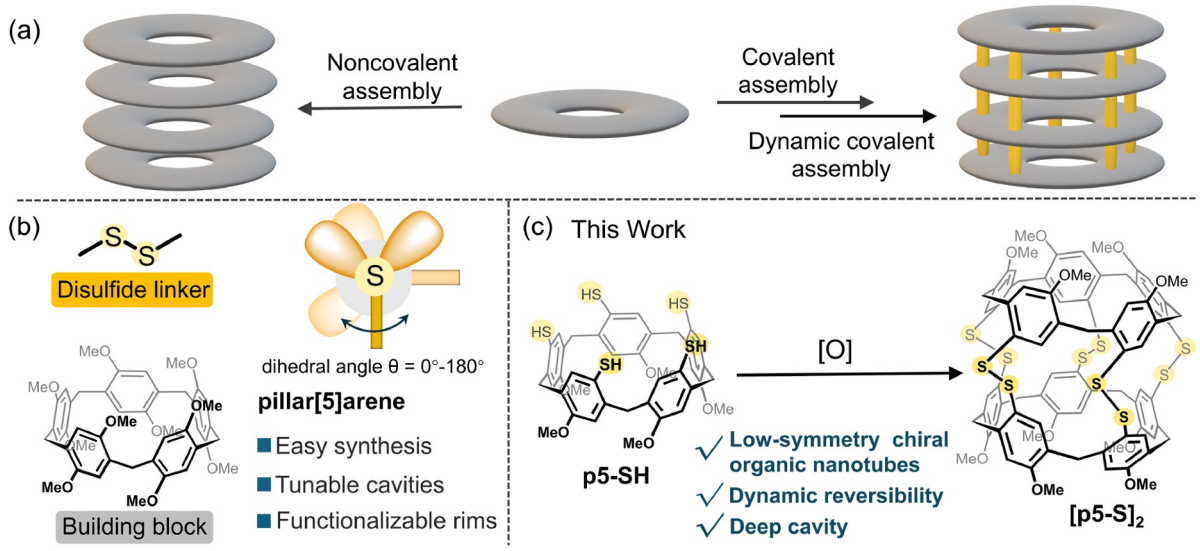

Figure 1 (Color online) Synthetic strategies for synthesizing organic nanotubes. (a) General approaches to organic nanotube synthesis. (b) Structural illustration and features of disulfide bond linkage and pillar[5]arene. (c) The dynamic covalent self-assembly and dimerization of monomer **p5-SH** enable the construction of low-symmetry chiral organic nanotubes.

constructing complex molecular architectures. Various macrocycles, including cyclodextrins [36–39], cyclotriveratrylenes [40,41], resorcinarenes [42–44], and calixarenes [45–47], are widely used as building blocks for nanotubes or capsules. Pillararenes [48] stand out from these macrocyclic hosts, emerging as versatile building blocks for supramolecular architectures [49–54], due to their ease of synthesis, tunable cavities and functionalizable rims [55–58] (Figure 1b). Rim-differentiated pillar[5]arenes (**p5**) [59–61] are especially promising for constructing chiral systems, as their asymmetric substitution patterns can enforce directional assembly [62,63]. A diverse range of chiral organic nanotubes has been constructed through dynamic imine bond bridging of **p5** [64–69]. However, the inherent preference of dynamic imine linkages to adopt a planar geometry hinders their application in the precise assembly of low-symmetry structures. In contrast, the tunable bond angles and chemical reversibility of dynamic disulfide linkages offer both stereochemical precision and structural flexibility, enabling the accurate synthesis of redox-responsive, low-symmetry assemblies.

Herein, we report a synthesis of chiral organic nanotubes through dynamic disulfide bridging of rim-differentiated pentathiol-functionalized pillar[5]arene (**p5-SH**) (Figure 1c). The building block **p5-SH** dimerizes under oxidative conditions to form a sulfur-containing nanotube, denoted as **[p5-S]$_2$**, bridged by five dynamic covalent disulfide bonds. X-ray crystal structure data revealed the structure of **[p5-S]$_2$** spans an overall length of 1.34 nm with a volume of approximately 212 Å^3. The cavity exhibits a low-symmetry chiral structure, arising from the conformation lock by covalent disulfide bond linkage, and a pair of enantiomers, namely, ***P′M*-[p5-S]$_2$** and ***M′P*-[p5-S]$_2$**, was found and isolated. Additionally, the dynamic reversibility of the covalent disulfide bonds in **[p5-S]$_2$** has been investigated, during which an unusual autocatalytic behavior was observed. Moreover, the deep cavity of the nanotube was found to provide a rigid space suitable for hosting linear guest molecules.

2 Results and discussion

2.1 Synthesis and crystal structure of p5-SH

The preparation of the penta-thiol-functionalized monomer **p5-SH** is essential for the successful synthesis of the dimerized nanotube **[p5-S]$_2$**. The synthesis of **p5-SH** starts with the known penta-phenolic compound **p5-OH** [70] and proceeds through three steps (Scheme 1). First, the five phenolic hydroxyl groups of **p5-OH** are esterified using *N*,*N*-dimethylthiocarbamoyl chloride (DMTCC), yielding the penta-thiocarbamoyl-substituted intermediate **p5-ODT**, which subsequently undergoes a Newman-Kwart rearrangement to form the penta-carbamothioate precursor **p5-SDT** upon heating under reflux in diphenyl ether for 16 h under a nitrogen atmosphere (Scheme S1, Figures S1–S4, Supporting Information online). Finally, the thiocarbamate groups are cleaved from **p5-SDT** by NaOH to give the target compound **p5-SH** with a 24% overall yield for three steps [71,72]. The ^{1}H NMR spectrum of **p5-SH** displays a simple pattern, reflecting high symmetry of the molecule in solution (Figures S5 and S6). High-resolution mass spectrometry (HRMS) (Figure S10) further confirms the identity of **p5-SH**.

https://www.sciengine.com/doi/10.1007/s11426-025-3087-0

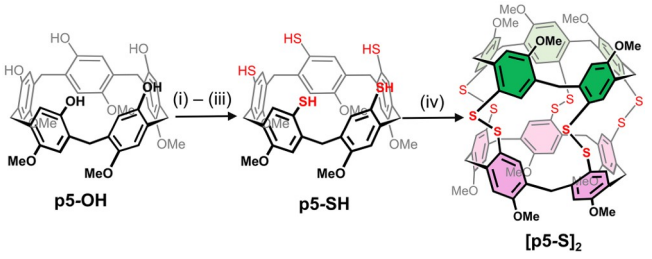

Scheme 1 (Color online) Synthesis route of **[p5-S]$_2$**. Reaction conditions: (i) DMTCC, Cs_2CO_3, acetone, N_2, 65 °C, 24 h, 54%. (ii) PhOPh, N_2, reflux, 16 h, 60%. (iii) NaOH, MeOH, THF, N_2, 40 °C; then HCl, H_2O, 70%. (iv) K_2CO_3, acetone, air, 60%.

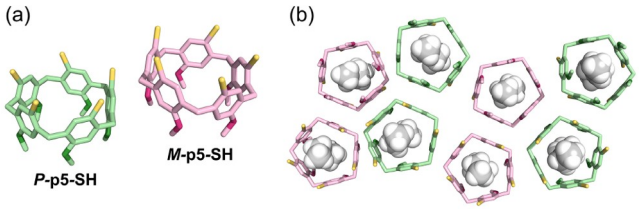

Figure 2 (Color online) X-ray crystal structures of **p5-SH**. (a) Side view of ***M*-p5-SH** and ***P*-p5-SH**. (b) Top view of the 2D packing mode of *n*-pentane⊂**p5-SH**. All hydrogens of **p5-SH** are omitted for the sake of clarity. Color code: green/pink/grey, carbon; dark green/dark pink, oxygen; yellow, sulfur; white, hydrogen.

To further verify the structure of **p5-SH**, single crystals were successfully obtained by slow vapor diffusion of *n*-pentane into a dichloromethane solution. The X-ray crystal structure reveals its C_5-symmetrical conformation and pillar-shaped cavity with a solvent molecule, *n*-pentane, occupied. Moreover, two distinct enantiomeric conformers, ***M*-p5-SH** and ***P*-p5-SH**, are observed in the solid state, adopting a zigzag arrangement next to each other in the crystal lattice (Figure 2).

2.2 Synthesis and stereochemistry of [p5-S]$_2$

Following the successful synthesis of **p5-SH**, the dimerization step was carried out by dissolving the monomer in an acetone solution containing potassium carbonate and stirring the mixture at room temperature under air for 12 h. During this process, a significant amount of precipitate, likely corresponding to oligomeric and polymeric byproducts, was observed to form. Upon completion of the reaction, the product was isolated by first removing the insoluble byproducts through filtration, and subsequently by recrystallization from a dichloromethane and methanol mixed solvent system, yielding the dimerized product **[p5-S]$_2$** with a 60% overall yield (Scheme 1, Figure S26). The ^{1}H NMR spectrum of **[p5-S]$_2$** presents a surprisingly complex pattern. For comparison, the spectrum of **p5-SH** displays only five singlets: two aromatic signals at δ 6.56 ppm and δ 7.17 ppm, along with the methylene signal at 3.88 ppm, the methoxy signal at 3.38 ppm, and the thiol signal at δ 3.22 ppm (Figure 3a). In contrast, the spectrum of **[p5-S]$_2$** shows the disappearance of the thiol signal, indicating the formation of disulfide bonds. The remaining signals, however, are significantly more complex, with the methoxy signal splitting into ten singlets and the aromatic signals splitting into twenty peaks (with some overlaps) (Figure 3b). ^{1}H diffusion-ordered spectroscopy (DOSY) NMR confirms that all signals belong to a single species, with a diffusion constant estimated to be 1.38×10^{-6} m^2/s (Figure 3c). HRMS clearly shows signals for **[p5-S]$_2$**, confirming its existence as a dimer (Figure 3d). The ^{1}H-^{1}H NOESY and ^{1}H-^{13}C HSQC spectra (Figures S13–S17) reveal that the aromatic proton signals of **[p5-S]$_2$** can be divided into two distinct groups corresponding to different aromatic environments: H_6 (near the center of the nanotube) and H_3 (close to the rim of the nanotube) (Figure 3e) which can be correlated with the two proton signals observed in the monomer. Combining these 2D NMR spectra with ^{1}H-^{13}C HMBC (Figures S18–S21), most signals in ^{1}H NMR (Figure S11) and ^{13}C NMR (Figure S12) can be assigned. Thus, based on the NMR and HRMS data, we conclude that **[p5-S]$_2$** is a dimer derivative formed by the oxidation of the monomer **p5-SH** under basic conditions. The dimer is linked by disulfide bonds, and its symmetry degrades from the C_5 symmetry of the monomer to C_1 symmetry in the dimer.

To further elucidate the structure of **[p5-S]$_2$**, we employed slow vapor diffusion of methanol into a solution of **[p5-S]$_2$** in a mixed solvent of *N*-methylpyrrolidone (NMP) and dichloromethane. The solution was allowed to stand undisturbed at room temperature for 20 d, yielding yellow plate-like single crystals. The X-ray crystal structure analysis confirmed that **[p5-S]$_2$** is a nanotube formed by the dimerization of **p5-SH** through five disulfide linkages (Figure 4). Additionally, the absence of any symmetry elements within the molecule further explains the low-symmetry ^{1}H NMR spectrum observed for **[p5-S]$_2$**. The geometry of the dimer molecule features a barrel-like shape, characterized by a broad central region and two narrow terminal ends. The total length of the nanotube from head to tail is 1.34 nm. The interior of the nanotube contains a continuous one-dimensional channel, occupied by two dichloromethane solvent molecules, with an estimated cavity volume of approximately 212 Å^3 (Figure 4a, b). The bond angles of the disulfide linkages range from 99.9° to 107.3°, while the dihedral angles (χ_1–χ_5) of the disulfide bonds are −116.5°, 123.7°, 111.2°, −116.4°, and 113.7°, respectively (Figure S36). In the crystal packing, **[p5-S]$_2$** molecules are arranged in a herringbone stacking pattern along the *a*-axis (Figure 4c). The methyl group of **[p5-S]$_2$** form intermolecular C–H···S hydrogen bonds with the disulfide bonds of neighboring molecules, with the H···S distance as short as 2.8 Å (Figure S38).

https://www.sciengine.com/doi/10.1007/s11426-025-3087-0

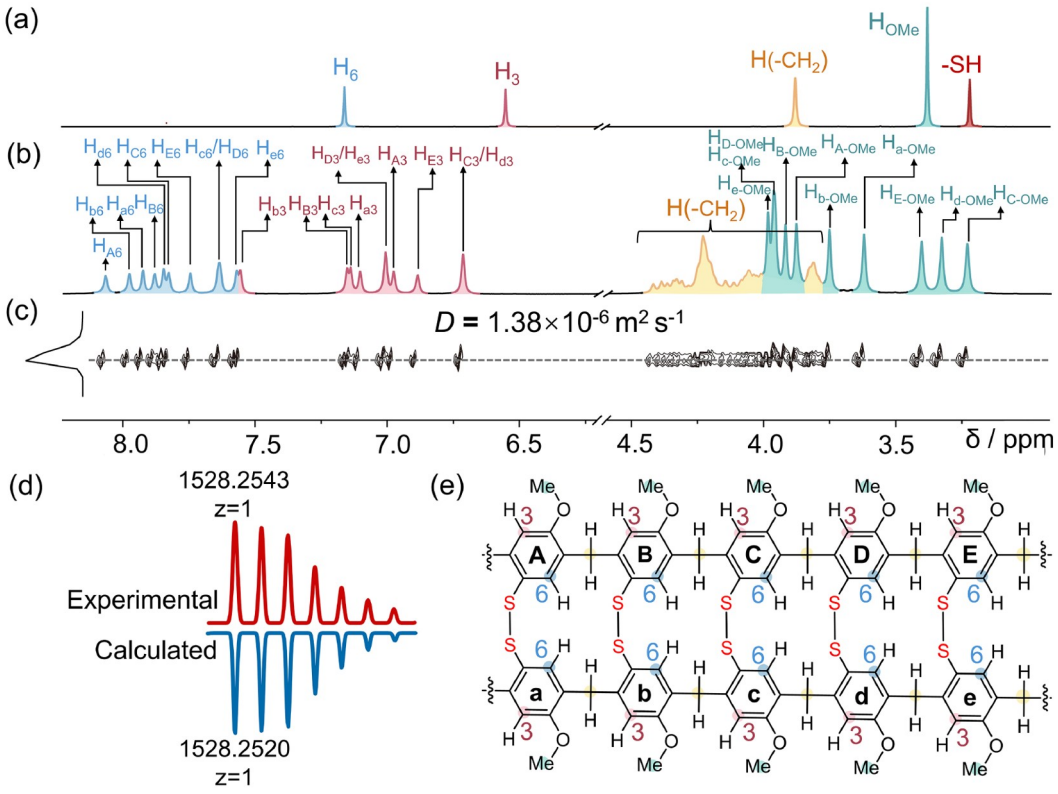

Figure 3 (Color online) Partial ^{1}H NMR spectra of (a) **p5-SH**, (b) **[p5-S]$_2$**, and (c) DOSY spectrum of **[p5-S]$_2$** (400 MHz, $C_2D_2Cl_4$, 298 K). (d) ESI-HR-MS (red) and simulated isotope pattern (blue) of **[p5-S]$_2$**. (e) Chemical formula illustration and labels of **[p5-S]$_2$**.

The formation of the dimer **[p5-S]$_2$** can theoretically yield two different structures with a pair of enantiomers being the homochiral ***MM*-[p5-S]$_2$** and ***PP*-[p5-S]$_2$**, as well as the heterochiral ***PM*-[p5-S]$_2$**, possibly being a *meso* compound. This arises from the fact that the monomer **p5-SH** exists as ***M*** and ***P*** chirality, which can interconvert via phenyl ring flipping in solution. However, once the dimer **[p5-S]$_2$** is formed through disulfide bond linkage, the inversion of its structural units is locked, thereby fixing its chirality. Interestingly, the X-ray crystallographic analysis revealed that dimerization only occurs in a heterochiral manner. Moreover, as indicated by the ^{1}H NMR spectroscopy, the dimer existed in a low-symmetry state with each half of the dimer residing in a distinct chemical environment. This observation was corroborated by the X-ray structure, which identified a pair of enantiomers (Figure 4d, Figure S39), instead of a *meso* compound, in the fashion that although each enantiomer is composed of a ***P*** monomer and an ***M*** monomer, the ***P*** and ***M*** counterparts are not mirror images of each other because of slightly different dihedral angles and bond angles locked by the conformation. Thus, they are precisely denoted as ***P'M*-[p5-S]$_2$** and ***M'P*-[p5-S]$_2$** [73].

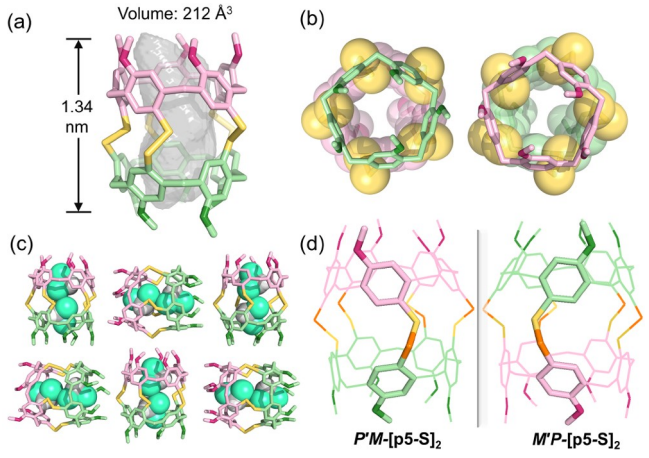

Figure 4 (Color online) X-ray crystal structures of **[p5-S]$_2$**. (a) Side view of **[p5-S]$_2$** illustrating the length of 1.34 nm and inner 1D channel volume of 212 Å^3. (b) Top and bottom view of **[p5-S]$_2$**. (c) Solid state superstructures of **[p5-S]$_2$** showing each molecule is hosting two dichloromethane solvent molecules in the cavity. (d) Illustration of a pair of enantiomers ***P'M*-[p5-S]$_2$** and ***M'P*-[p5-S]$_2$**. All hydrogens are omitted for the sake of clarity. Color code: green/pink, carbon; dark green/dark pink, oxygen; yellow/orange, sulfur.

To gain deeper insight into the conformational preferences, density functional theory (DFT) calculations were employed (Figure S41). Specifically, the structures of the homochiral dimer ***M'M*-[p5-S]$_2$** and the heterochiral dimer ***P'M*-[p5-S]$_2$** were optimized, and their corresponding energies were calculated. The results revealed that ***M'M*-[p5-S]$_2$** exhibits a

https://www.sciengine.com/doi/10.1007/s11426-025-3087-0

higher energy by 95.9 kJ/mol compared to ***P′M*-[p5-S]$_2$**, suggesting that the heterochiral dimer is thermodynamically more stable (Figure 5). This finding rationalizes the selective dimerization behavior observed in our experiments and can be attributed to the preferred torsion of the disulfide bonds. While the dihedral angles of disulfide bonds in proteins can span from 0° to 180°, the stable C–S–S–C dihedral angle [74,75] typically approaches 90°. This torsional preference likely drives the formation of the more stable heterochiral dimer. In the solid state, the dihedral angles of ***P′M*-[p5-S]$_2$** and ***M′P*-[p5-S]$_2$** fall between 111.2° and 123.7°, whereas the optimized structure of ***M′M*-[p5-S]$_2$** contains two large angles of approximately 170°, which significantly deviate from the stable conformation of 90°, leading to considerable strain and thus reducing its stability.

The pair of enantiomers ***P′M*-[p5-S]$_2$** and ***M′P*-[p5-S]$_2$** was successfully separated using chiral high-performance liquid chromatography (HPLC) (Figure S28). In the chiral HPLC analysis, two distinct fractions (Figure 6a) were observed, both of which exhibited identical ^{1}H NMR spectra (Figure S29), suggesting that these two fractions are a pair of enantiomers. The electronic circular dichroism (ECD) spectra of the enantiomers exhibit mirror-image Cotton effects (Figure 6b). In the UV-vis spectra, both enantiomers display identical patterns, featuring an absorption band centered around 265 nm (Figure S31).

To investigate the structural stability of **[p5-S]$_2$**, variable-temperature ^{1}H NMR spectra were recorded over a temperature range from 298 to 403 K (Figure S32). Upon heating a 1,1,2,2-tetrachloroethylene-d_2 solution of **[p5-S]$_2$** to 363 K, the low symmetry nature of the proton signals pattern remained unchanged, indicating that the elevated temperature did not affect the structure of **[p5-S]$_2$**. Even when the temperature was further increased to 403 K, the spectra did not revert to a high symmetry pattern. Moreover, the ^{1}H NMR spectrum fully recovered to the original form when the sample was cooled back to 298 K, demonstrating the strong thermal stability of **[p5-S]$_2$**.

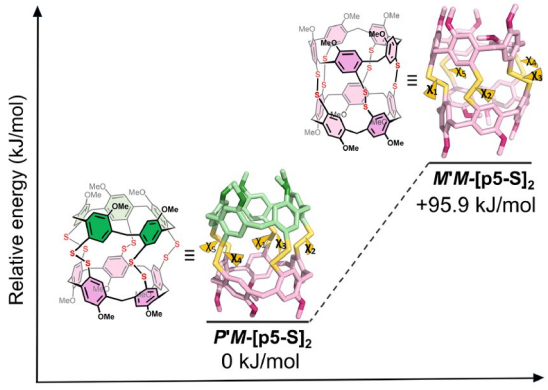

Figure 5 (Color online) Calculated relative energies of ***P′M*-[p5-S]$_2$** and its homochiral diastereomer ***M′M*-[p5-S]$_2$**. The dihedral angles (χ_1–χ_5) in ***P′M*-[p5-S]$_2$** are −116.5°, 123.7°, 111.2°, −116.4°, and 113.7°, respectively, while the dihedral angles in ***M′M*-[p5-S]$_2$** are 169.4°, 122.8°, 173.4°, 91.5°, and 93.3°, respectively.

2.3 Reversible redox conversion

The reversible redox interconversion between the monomer **p5-SH** and the dimer **[p5-S]$_2$**, driven by the reversibility of the dynamic covalent disulfide bond, was further investigated in detail. The oxidation process was studied first, where **p5-SH** was dissolved in a chloroform-*d* solution, treated with triethylamine, and exposed to air at room temperature. The oxidative dimerization of **p5-SH** was monitored by ^{1}H NMR spectroscopy (Figure 7a). As the reaction progressed, the signals of **p5-SH** gradually decreased, while new signals from **[p5-S]$_2$** appeared, indicating that the monomer was progressively converted into a dimer. The signal intensity for **[p5-S]$_2$** remained constant after 19 d due to the limited solubility of **[p5-S]$_2$** in $CDCl_3$, as evidenced by the formation of a precipitate in the NMR tube. Approximately 97% of **p5-SH** was consumed after 39 d (Figures S45–S47) and the concentration changes of **p5-SH** over time in the oxidation reaction were found to follow the first-order kinetic model. To demonstrate the reversibility of the redox reaction between **p5-SH** and **[p5-S]$_2$**, dithiothreitol (DTT)

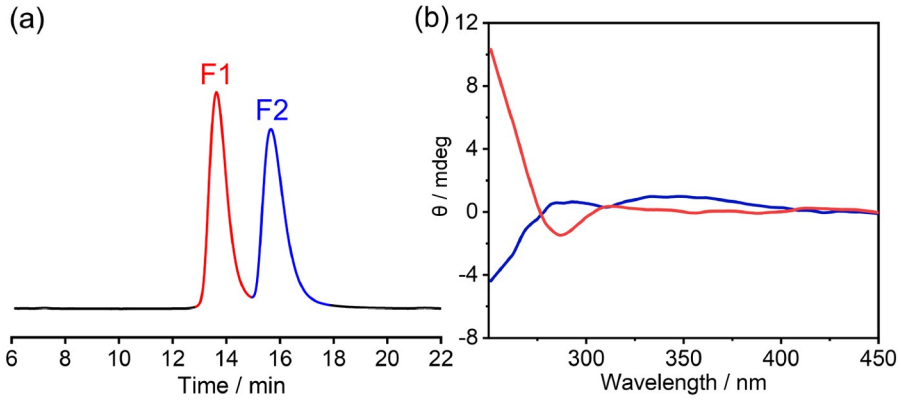

Figure 6 (Color online) (a) Partial HPLC chromatograms (UV detection wavelength at 280 nm) of racemic **[p5-S]$_2$**. (b) ECD spectra of two HPLC-resolved fractions recorded at 0.036 mM (red) and 0.043 mM (blue) in CH_2Cl_2 solution.

https://www.sciengine.com/doi/10.1007/s11426-025-3087-0

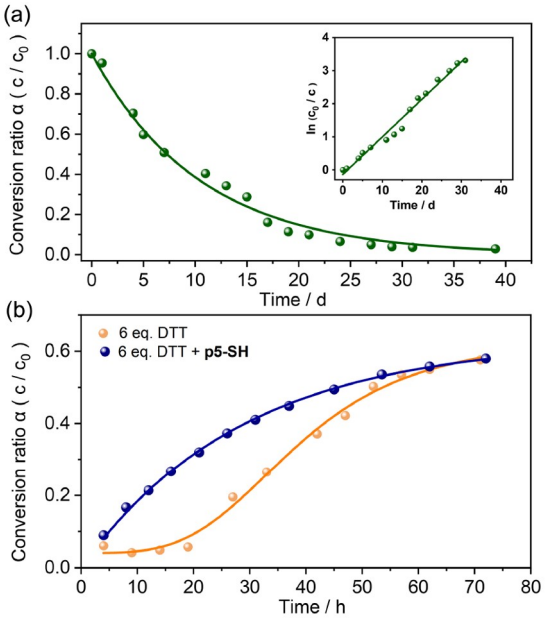

Figure 7 (Color online) (a) Kinetic plot of oxidative self-dimerization indicated by the conversion rate of **p5-SH** with nonlinear curve-fitting. The inset shows the linear relationship of $\ln(c_0/c)$ *versus* time, indicating first-order kinetics. **p5-SH** (10 mg) was dissolved in $CDCl_3$ (0.55 mL), then Et_3N (0.50 μL) was added. The reaction was exposed to air and stood at room temperature. (b) Kinetic plot of the reduction process with nonlinear curve-fitting. Orange: autocatalytic feature of the reduction process. **[p5-S]$_2$** (5 mg) was dissolved in $C_2D_2Cl_4$ (0.80 mL), then (dithiothreitol) DTT (3.0 mg, 6 eq.) and K_2CO_3 (5 mg) were added. Blue: **p5-SH**-catalyzed reaction kinetics. **[p5-S]$_2$** (5 mg) was dissolved in $C_2D_2Cl_4$ (0.80 mL), then DTT (3.0 mg, 6.0 eq.), K_2CO_3 (5 mg) and **p5-SH** (2.5 mg) were added.

was added to a 1,1,2,2-tetrachloroethylene-d_2 solution containing **[p5-S]$_2$** and potassium carbonate. The reduction process was monitored by ^{1}H NMR spectroscopy. After 71 h, 58% of **[p5-S]$_2$** was reduced to its monomer form (Figures S48–S50). Interestingly, unlike the first-order kinetics for the oxidation of **p5-SH**, the reverse process exhibited more complex kinetics. Only a trace amount of **p5-SH** was detected and remained almost unchanged during the first 20 h. Subsequently, the formation rate of **p5-SH** increased sharply, reaching near-maximal conversion within the next 10 h. The overall reaction rate followed a slow-fast-slow trend, with an S-shaped kinetic profile (Figure 7b), indicative of an autocatalytic reaction. ^{1}H NMR spectra revealed that upon adding DTT, the original signals of **[p5-S]$_2$** disappeared and were replaced by a new set of signals, including highly shielded proton signals below 0 ppm. This suggests the formation of a host-guest complex between DTT and **[p5-S]$_2$** with slow exchange dynamics on the NMR time scale. Further ^{1}H NMR spectroscopic titration experiments (Figure S51) confirmed the host-guest complex with a binding constant of $(3.65 \pm 0.34) \times 10^4$ M^{-1}. In contrast, the interaction between DTT and **p5-SH** involved fast exchange, showing a much smaller binding constant of (36.4 ± 0.5) M^{-1} (Figures S52–S54). The significant difference in host-guest behavior between DTT and the host in its dimer form or monomer form led us to initially propose that the induction period was due to the stronger host-guest binding between DTT with **[p5-S]$_2$**. However, adding a large excess of DTT accelerated the reaction while still preserving its autocatalytic nature (Figures S55–S57), thus rejecting our initial hypothesis. Subsequently, adding one equivalent of **p5-SH** to the reaction mixture significantly accelerated the initial reaction rate, eliminated the induction period, and converted the kinetic profile from sigmoidal to normal exponential decay (Figure 7b), as monitored by real-time ^{1}H NMR spectroscopy (Figures S58–S61).

To evaluate the effect of **p5-SH** on the reduction rate of **[p5-S]$_2$**, 4-methoxybenzenethiol (structural unit of **p5-SH**) was used as a control. Unlike the **p5-SH**-mediated reaction, the control reaction showed a clear induction period and sigmoidal kinetics (Figures S62–S64). The catalytic activity of **p5-SH** was further examined using 4-methoxyphenyl disulfide as substrate. **p5-SH** significantly accelerated its reductive decomposition (Figures S65–S68). A disulfide exchange mechanism, consistent with the catalytic behavior observed in 4-methoxyphenyl disulfide reduction, was proposed and verified by ESI-HR-MS (Figures S69 and S70). These findings demonstrate that **p5-SH**, released through dimer dissociation, acts as an efficient catalyst to the reductive process, likely via a thiol-disulfide exchange mechanism (Figure S71) [32]. The cycle is initiated when **p5-S**$^-$ attacks the disulfide bond of 4-methoxyphenyl disulfide, cleaving it and forming an intermediate. The resulting species is then reduced by DTT to regenerate **p5-SH**, enabling its participation in subsequent catalytic cycles. Based on this evidence, it is proposed that the autocatalytic reduction of **[p5-S]$_2$** also operates through a disulfide exchange.

2.4 Host-guest properties

The electron-rich cavity of **p5** is able to form complexes with *n*-alkanes through C–H···π interactions [55]. The **[p5-S]$_2$** benefits from the synergistic effects of two **p5** cavities, exhibiting a deeper π-electron-rich cavity with a rigid low low-symmetric shape, thereby enhancing its ability to recognize and bind linear guest molecules in solution. The host-guest interactions and binding constants (K_a) of **[p5-S]$_2$** with various linear guests, including *n*-alkanes in different lengths, α, ω-dibromoalkanes and α,ω-dicyanides, were evaluated using ^{1}H NMR spectroscopy (Table S3, Supporting Information online). Due to the low solubility of **[p5-S]$_2$** in many common solvents, 1,1,2,2-tetrachloroethylene-d_2 was selected as the solvent for host-guest studies. The complexation of **[p5-S]$_2$** with *n*-hexane was first investigated using ^{1}H NMR spectroscopy. Upon mixing **[p5-S]$_2$** with *n*-hexane, a new set of peaks emerged, with some signals appearing in the high-shielding region ($\delta < 0$ ppm). Meanwhile, the original signals

https://www.sciengine.com/doi/10.1007/s11426-025-3087-0

of **[p5-S]$_2$** remained largely unchanged, indicating the formation of a host-guest complex with slow exchange of the free guest on the NMR timescale (Figure 8a). This behavior is likely attributed to the small opening of the deep cavity of **[p5-S]$_2$**, which facilitates strong C–H···π interactions within the host-guest complex. ^{1}H NMR titration experiments (Figure S73) revealed a binding constant K_a = (5.9 ± 0.63) ×10^3 M^{-1}.

To investigate how the chain length of *n*-alkanes affects their binding ability with **[p5-S]$_2$**, *n*-heptane, *n*-octane, *n*-nonane, as well as *n*-pentane were tested to form host-guest complexes with **[p5-S]$_2$** (Figure 8b). Similar slow exchange behaviors on the NMR timescale were observed for these complexes as seen with *n*-hexane⊂**[p5-S]$_2$**. The complexations of these *n*-alkane guests with **[p5-S]$_2$** host were all probed by ^{1}H NMR titration experiments (Figure 8c). For the shorter linear alkane *n*-pentane, the K_a value significantly decreased to (1.9 ± 0.38) × 10^3 M^{-1} (Figure S72), indicating a lower binding affinity with **[p5-S]$_2$** compared to *n*-hexane. In the case of longer *n*-heptane, the binding constant was determined to be (4.3± 0.55) × 10^3 M^{-1} (Figure S74), slightly lower than that of *n*-hexane. As the chain length increases further to *n*-octane and *n*-nonane, the binding constants decreased to (2.5 ± 0.33) × 10^3 and (4.3 ± 1.3) × 10^2 M^{-1} (Figures S75 and S76), respectively, indicating that the binding affinity diminishes with longer alkanes. No significant binding was detected by ^{1}H NMR spectroscopy when the chain length reached *n*-decane. Thus, *n*-hexane exhibits the highest binding affinity with **[p5-S]$_2$** among these linear alkanes, likely because its length matches the cavity of **[p5-S]$_2$**. The electrostatic potential map shows that the inner surface of the deep cavity is predominantly electron-deficient, while the ends are electron-rich (Figure S42). Therefore, 1,4-dicyanobutane and 1,6-dibromohexane, with the same carbon number as *n*-hexane but with electron-withdrawing groups at both ends, were selected as guests. These guests match both the shape and electron density with the **[p5-S]$_2$** cavity. Similarly, both 1,6-dibromohexane and 1,4-dicyanobutane exhibit slow exchange on the NMR timescale with **[p5-S]$_2$**, but with significantly stronger binding affinities compared with *n*-hexane, exhibiting binding constants of (1.0 ± 0.26) × 10^5 and (1.3 ± 0.29) × 10^5 M^{-1}, respectively (Figures S78 and S79).

3 Conclusions

In summary, we successfully synthesized a pillar[5]arene derivative, **p5-SH**, bearing five thiol groups at the same rim, and confirmed its high symmetry using NMR spectroscopy and X-ray crystallography. By leveraging the dynamic properties of disulfide bonds, we achieved its dimerization into a covalently linked **[p5-S]$_2$** by NMR spectroscopy and X-ray crystallography revealed its unique low-symmetry heterochiral dimeric structure. A pair of enantiomers, ***P′M*-[p5-S]$_2$** and ***M′P*-[p5-S]$_2$**, is identified and separated. Kinetic analysis of the reversible redox processes governing the dissociation of **[p5-S]$_2$** showed an autocatalytic behavior, where the released **p5-SH** accelerates the reduction reaction, underscoring the dynamic role of disulfide bonds in supra-

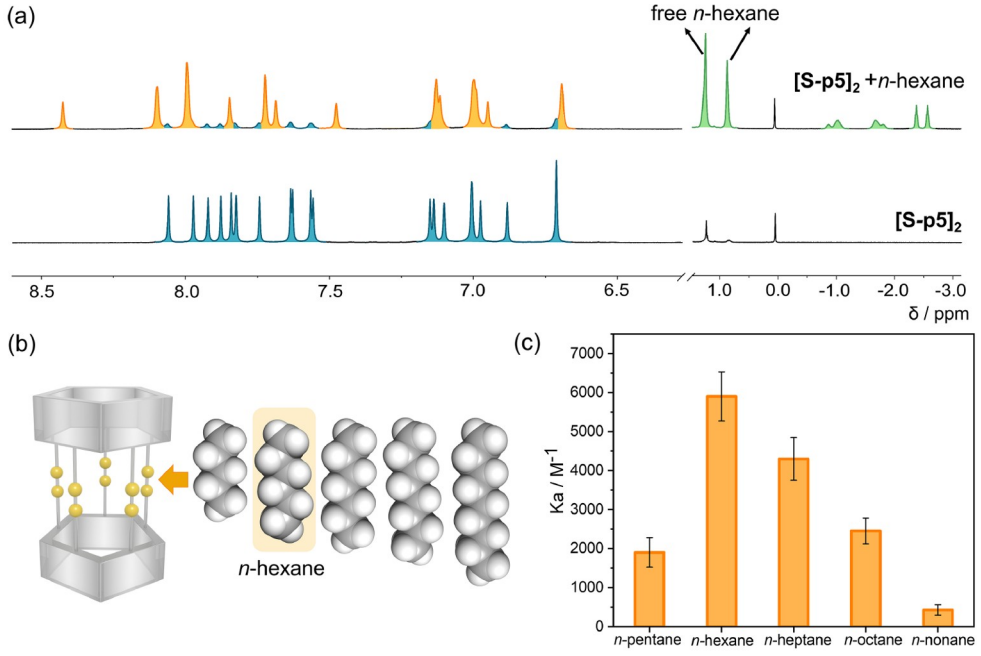

Figure 8 (Color online) (a) ^{1}H NMR spectra (400 MHz, $C_2D_2Cl_4$, 298 K) of **[p5-S]$_2$** (bottom) and **[p5-S]$_2$** with 2.0 eq. *n*-hexane (top). (b) Linear alkane guests used for complexation with **[p5-S]$_2$**. (c) Binding constants (K_a) of **[p5-S]$_2$** with linear alkane guests determined by ^{1}H NMR methods in $C_2D_2Cl_4$ at 298 K.

https://www.sciengine.com/doi/10.1007/s11426-025-3087-0

molecular chemistry. Additionally, the barrel-like cavity of **[p5-S]$_2$** efficiently hosts various linear guest molecules, demonstrating potential applications in materials science and nanotechnology. This work offers an innovative molecular design strategy and provides valuable insights for constructing diverse low-symmetry chiral tubular structures, advancing the field of supramolecular architecture and functional nanomaterials.

Acknowledgements This work was supported by the Fundamental Research Funds for the Central Universities, and the National Natural Science Foundation of China (NSFC) (22171193). We thank Lizhi Fang, Jingyu Ma, and Prof. Cheng Yang at Sichuan University for their help with chiral HPLC spectrum, UV-Vis spectra and electronic circular dichroism spectra. We thank Zhengbin Tang and Prof. Zhichang Liu at Westlake University for their help with variable temperature ^{1}H NMR spectra. We thank Dr. Jing Li and Dr. Dongyan Deng from Sichuan University for HRMS and NMR testing, respectively.

Conflict of interest The authors declare no conflict of interest.

Supporting information The supporting information is available online at http://chem.scichina.com and http://link.springer.com/journal/11426. The supporting materials are published as submitted, without typesetting or editing. The responsibility for scientific accuracy and content remains entirely with the authors.

1 Shimizu T, Ding W, Kameta N. *Chem Rev*, 2020, 120: 2347–2407
2 Cao Q, Rogers JA. *Adv Mater*, 2009, 21: 29–53
3 Zhou SS, Shi XL, Li L, Liu Q, Hu BX, Chen WY, Zhang CY, Liu QF, Chen ZG. *Adv Mater*, 2025, 37: 2347–2407
4 Kong J, Franklin NR, Zhou C, Chapline MG, Peng S, Cho K, Dai H. *Science*, 2000, 287: 622–625
5 Schroeder V, Savagatrup S, He M, Lin S, Swager TM. *Chem Rev*, 2018, 119: 599–663
6 Ackermann J, Metternich JT, Herbertz S, Kruss S. *Angew Chem Int Ed*, 2022, 61: e202112372
7 Saji VS. *Mater Today Adv*, 2022, 14: 100239
8 Kumar S, Rani R, Dilbaghi N, Tankeshwar K, Kim KH. *Chem Soc Rev*, 2017, 46: 158–196
9 Iijima S. *Nature*, 1991, 354: 56–58
10 Segawa Y, Yagi A, Matsui K, Itami K. *Angew Chem Int Ed*, 2016, 55: 5136–5158
11 Yang F, Wang M, Zhang DQ, Yang J, Zheng M, Li Y. *Chem Rev*, 2020, 120: 2693–2758
12 He MS, Zhang SC, Zhang J. *Chem Rev*, 2020, 120: 12592–12684
13 Bong DT, Clark TD, Granja JR, Ghadiri MR. *Angew Chem Int Ed*, 2001, 40: 988–1011
14 Balbo Block MA, Kaiser C, Khan A, Hecht S. *Top Curr Chem*, 2005, 245: 89–150
15 Roy A, Joshi H, Ye R, Shen J, Chen F, Aksimentiev A, Zeng HQ. *Angew Chem Int Ed*, 2020, 59: 4806–4813
16 Fu YH, Hu YF, Lin T, Zhuang GW, Wang YL, Chen WX, Li ZT, Hou JL. *Nat Chem*, 2024, 16: 1418–1426
17 Nitti A, Pacini A, Pasini D. *Nanomaterials*, 2017, 7: 167
18 Zhang W, Jin WS, Fukushima T, Saeki A, Seki S, Aida T. *Science*, 2011, 334: 340–343
19 Maeda K, Hong L, Nishihara T, Nakanishi Y, Miyauchi Y, Kitaura R, Ousaka N, Yashima E, Ito H, Itami K. *J Am Chem Soc*, 2016, 138: 11001–11008
20 Strauss MJ, Asheghali D, Evans AM, Li RL, Chavez AD, Sun C, Becker ML, Dichtel WR. *Angew Chem Int Ed*, 2019, 58: 14708–14714
21 Chamorro PB, Aparicio F. *Chem Commun*, 2021, 57: 12712–12724
22 González-Sánchez M, Mayoral MJ, Vázquez-González V, Paloncýová M, Sancho-Casado I, Aparicio F, de Juan A, Longhi G, Norman P, Linares M, González-Rodríguez D. *J Am Chem Soc*, 2023, 145: 17805–17818
23 Sun Z, Ikemoto K, Fukunaga TM, Koretsune T, Arita R, Sato S, Isobe H. *Science*, 2019, 363: 151–155
24 Li K, Yoshida S, Yakushiji R, Liu XC, Ge C, Xu ZF, Ni Y, Ma XN, Wu JS, Sato S, Sun Z. *Chem Sci*, 2024, 15: 18832–18839
25 Neuhaus P, Cnossen A, Gong JQ, Herz LM, Anderson HL. *Angew Chem Int Ed*, 2015, 54: 7344–7348
26 Mao LL, Xiao H, Zhao JQ, Diao Z, Zhou W, Li H, Tung CH, Wu LZ, Cong H. *CCS Chem*, 2022, 4: 3772–3780
27 Rowan SJ, Cantrill SJ, Cousins GRL, Sanders JKM, Stoddart JF. *Angew Chem Int Ed*, 2002, 41: 898–952
28 Jin YH, Yu C, Denman RJ, Zhang W. *Chem Soc Rev*, 2013, 42: 6634
29 Koner K, Karak S, Kandambeth S, Karak S, Thomas N, Leanza L, Perego C, Pesce L, Capelli R, Moun M, Bhakar M, Ajithkumar TG, Pavan GM, Banerjee R. *Nat Chem*, 2022, 14: 507–514
30 Cougnon FBL, Stefankiewicz AR, Ulrich S. *Chem Sci*, 2024, 15: 879–895
31 Orrillo AG, Furlan RLE. *Angew Chem Int Ed*, 2022, 61: e202201168
32 Black SP, Sanders JKM, Stefankiewicz AR. *Chem Soc Rev*, 2014, 43: 1861–1872
33 Sun CL, Xu JF, Chen YZ, Niu LY, Wu LZ, Tung CH, Yang QZ. *Polym Chem*, 2016, 7: 2057–2061
34 Lyu Y, Hu Y, Yang JH, Wang X, Li JW. *Angew Chem Int Ed*, 2024, 63: e202412020
35 Vial L, Perret F, Leclaire J. *Eur J Org Chem*, 2022, 2022: e202101274
36 Wang A, Li W, Zhang P, Ling CC. *Org Lett*, 2011, 13: 3572–3575
37 Kogame-Asahara C, Ito S, Iguchi H, Kazama A, Shigemitsu H, Kida T. *Chem Commun*, 2020, 56: 1353–1356
38 Shi L, Zhao W, Jiu Z, Guo J, Zhu Q, Sun Y, Zhu B, Chang J, Xin P. *Angew Chem Int Ed*, 2024, 63: e202403667
39 Jiang ZY, Chen Z, Yu XJ, Lu S, Xu WM, Yu B, Stern CL, Li SY, Zhao Y, Liu XZ, Han YQ, Chen SQ, Cai K, Shen DK, Ma KK, Li XP, Chen AXY. *J Am Chem Soc*, 2025, 147: 7325–7335
40 Brotin T, Dutasta JP. *Chem Rev*, 2009, 109: 88–130
41 Little MA, Donkin J, Fisher J, Halcrow MA, Loder J, Hardie MJ. *Angew Chem Int Ed*, 2012, 51: 764–766
42 Cram DJ, Karbach S, Kim YH, Baczynskyj L, Kallemeyn GW. *J Am Chem Soc*, 1985, 107: 2575–2576
43 Naumann C, Place S, Sherman JC. *J Am Chem Soc*, 2002, 124: 16–17
44 Kobayashi K, Yamanaka M. *Chem Soc Rev*, 2015, 44: 449–466
45 Chen FY, Li CZ, Han H, Geng WC, Zhang S, Jiang ZX, Zhao QY, Cai K, Guo DS. *Angew Chem Int Ed*, 2024, 63: e202402139
46 Kumar R, Sharma A, Singh H, Suating P, Kim HS, Sunwoo K, Shim I, Gibb BC, Kim JS. *Chem Rev*, 2019, 119: 9657–9721
47 Guo DS, Liu Y. *Chem Soc Rev*, 2012, 41: 5907–5921
48 Ogoshi T, Kanai S, Fujinami S, Yamagishi T, Nakamoto Y. *J Am Chem Soc*, 2008, 130: 5022–5023
49 Wu YT, Shi L, Xu L, Ying JL, Miao XH, Hua B, Chen ZJ, Sessler JL, Huang FH. *Nature*, 2025, 640: 676–682
50 Strutt NL, Fairen-Jimenez D, Iehl J, Lalonde MB, Snurr RQ, Farha OK, Hupp JT, Stoddart JF. *J Am Chem Soc*, 2012, 134: 17436–17439
51 Li ZY, Zhang Y, Zhang CW, Chen LJ, Wang C, Tan H, Yu Y, Li X, Yang HB. *J Am Chem Soc*, 2014, 136: 8577–8589
52 Wang K, Zhang R, Song Z, Zhang K, Tian X, Pangannaya S, Zuo M, Hu XY. *Adv Sci*, 2023, 10: 2206897
53 Liang B, Cheng YJ, Liu X, Jia L, Wei XH, Zheng Q, Wang P, Xia D, Yan XZ. *Sci China Chem*, 2024, 67: 3373–3381
54 Xu WT, Li X, Xu XQ, Wang XQ, Yang HB, Wang W. *Sci China Chem*, 2024, 67: 4202–4211
55 Ogoshi T, Yamagishi T, Nakamoto Y. *Chem Rev*, 2016, 116: 7937–8002
56 Kato K, Fa SX, Ogoshi T. *Angew Chem Int Ed*, 2023, 62: e202308316

https://www.sciengine.com/doi/10.1007/s11426-025-3087-0

57 Zhao T, Wu WH, Yang C. *Chem Commun*, 2023, 59: 11469–11483
58 Xue YT, Zeng Y, Shi YF, Tian Y, Sun CP, Zhang N, Zheng XY, Chen PK. *Sci China Chem*, 2025, 68: 3100–3107
59 Guo M, Wang X, Zhan C, Demay-Drouhard P, Li W, Du K, Olson MA, Zuilhof H, Sue ACH. *J Am Chem Soc*, 2018, 140: 74–77
60 Yang W, Samanta K, Wan X, Thikekar TU, Chao Y, Li S, Du K, Xu J, Gao Y, Zuilhof H, Sue ACH. *Angew Chem Int Ed*, 2020, 59: 3994–3999
61 Du K, Demay-Drouhard P, Samanta K, Li S, Thikekar TU, Wang H, Guo M, van Lagen B, Zuilhof H, Sue ACH. *J Org Chem*, 2020, 85: 11368–11374
62 Fa SX, Shi TH, Akama S, Adachi K, Wada K, Tanaka S, Oyama N, Kato K, Ohtani S, Nagata Y, Akine S, Ogoshi T. *Nat Commun*, 2022, 13: 7378
63 Wan XT, Li SS, Tian YR, Xu J, Shen LC, Zuilhof H, Zhang MM, Sue ACH. *Chem*, 2022, 8: 2136–2147
64 Shi TH, Fa SX, Nagata Y, Wada K, Ohtani S, Kato K, Ogoshi T. *Cell Rep Phys Sci*, 2022, 3: 101173
65 Shi TH, Nagata Y, Akine S, Ohtani S, Kato K, Ogoshi T. *J Am Chem Soc*, 2022, 144: 23677–23684
66 Tian YR, Guo YL, Dong X, Wan XT, Cheng KH, Chang R, Li SS, Cao XY, Chan YT, Sue ACH. *Nat Synth*, 2023, 2: 395–402
67 Zhang M, Gao S, Dong X, Sue ACH. *Tetrahedron Lett*, 2023, 126: 154642
68 Gao SN, Guo YL, Xue JF, Dong X, Cao XY, Sue ACH. *J Am Chem Soc*, 2024, 146: 20963–20971
69 Gao SN, Zhang M, Zhang YM, Wang CS, Sue ACH. *Angew Chem Int Ed*, 2025, 64: e202509177
70 Demay-Drouhard P, Du K, Samanta K, Wan X, Yang W, Srinivasan R, Sue ACH, Zuilhof H. *Org Lett*, 2019, 21: 3976–3980
71 Jin JJ, Miao JR, Cheng CY. *Chem Commun*, 2021, 57: 7950–7953
72 Luo JW, Guo YL, Li P, Sue ACH, Cheng CY. *Chem Commun*, 2022, 58: 8646–8649
73 The heterochiral dimers are designated as ***P′M*-[p5-S]$_2$** and ***M′P*-[p5-S]$_2$**, where the prime symbol (′) signifies a different conformation, which serves to differentiate these dimers from the *meso*-form ***PM*-[p5-S]$_2$**
74 Armstrong DA, Kaas Q, Rosengren KJ. *Chem Sci*, 2018, 9: 6548–6556
75 Haworth NL, Gready JE, George RA, Wouters MA. *Mol Simul*, 2007, 33: 475–485

https://www.sciengine.com/doi/10.1007/s11426-025-3087-0